

# Novel insights on the Coma Cluster kinematics with DESI. I. Linking mass profile, orbital anisotropy and galaxy populations

S. Pedratti<sup>1\*</sup>, L. Pizzuti<sup>1,2</sup>, M. Fossati<sup>1,3</sup>, A. Biviano<sup>2,4</sup>, A. Boselli<sup>5</sup>, A. Ragagnin<sup>2</sup>, A. Carlin<sup>1</sup>

<sup>1</sup> Dipartimento di Fisica G. Occhialini, Università di Milano-Bicocca, Piazza della Scienza 3, 20126 Milano, Italy

<sup>2</sup> INAF - Osservatorio Astronomico di Trieste, via G. Tiepolo 11, I-34143 Trieste, Italy

<sup>3</sup> INAF - Osservatorio Astronomico di Brera, via Brera 28, 20121 Milano, Italy

<sup>4</sup> IFPU – Institute for Fundamental Physics of the Universe, via Beirut 2, 34014 Trieste, Italy

<sup>5</sup> Aix Marseille Univ, CNRS, CNES, LAM, Marseille, France\*\*

Received XXXX

## ABSTRACT

We investigate the kinematic properties of the Coma galaxy cluster using a new, large, spectroscopic sample of member galaxies, from the Dark Energy Spectroscopic Instrument (DESI). By means of the MG-MAMPOSST code, which is based on the Jeans equation, we jointly reconstruct the total cluster mass profile and the velocity anisotropy profile. Assuming a Navarro-Frenk-White model, we estimate a virial mass  $M_{200} = 1.08^{+0.08}_{-0.09}$  (stat)  $\pm 0.09$  (syst)  $\times 10^{15} M_{\odot}$ , corresponding to  $r_{200} = 2.12 \pm 0.06$  Mpc and a scale radius for the mass profile  $r_s = 0.48^{+0.27}_{-0.13}$  Mpc, which provides the tightest robust kinematic mass profile constraint up-to-date. By considering separately the mass of the hot gas and the galaxy stellar mass, we further determine the dark matter mass profile, with  $M_{200}^{\text{DM}} = 8.6^{+1.2}_{-0.8} \times 10^{14} M_{\odot}$ . We discuss the impact of the mass and number density parametrisations, the effect induced by different choices of the cluster's rest frame and of the radial range of the kinematic analysis, further comparing our results with previous estimates from the literature. The cluster dynamical state has also been assessed, using the spatial and line-of-sight velocity distributions of the members.

We further perform a kinematic study of different subsamples of galaxy populations, selected based on their colour (red sequence, green valley, and blue cloud), focusing in particular on the anisotropy profiles and line-of-sight velocity distributions. The orbits of green valley and blue cloud galaxies appear to be more radial in the centre and in the outskirts, respectively, with the latter predicting a higher cluster virial mass.

This study provides new insights on the interplay between dynamical and intrinsic properties of galaxies in massive structures, fundamental to verify the tight connection between galaxy evolution and their environment.

**Key words.** Galaxy: evolution – galaxies: clusters: individual: Coma – galaxies: kinematics and dynamics

## 1. Introduction

Galaxy clusters, the largest gravitationally-bound systems in the Universe, are excellent laboratories at the crossroads of cosmology and astrophysics. In order to employ clusters as reliable cosmological probes, it is essential to use robust methods to estimate their total mass, as well as the radial mass distribution. These can provide fundamental insights on the dark matter properties (e.g. Biviano et al. 2023a; Vallés-Pérez et al. 2025) and the nature of gravity (e.g. Pizzuti et al. 2022; Zamani et al. 2024).

In parallel, the deep potential wells of galaxy clusters make them particularly convenient to study the processes affecting galaxy evolution and feedback scenarios in dense environments (e.g. Boselli et al. 2014, 2022; Sampaio et al. 2024). In particular, galaxy populations in clusters are predominantly composed of massive, red, quiescent galaxies with low star formation rates, generally referred to as 'Early-Type' galaxies (ETGs), alongside a smaller population of low-mass, blue, highly star-forming galaxies, known as 'Late-Type' galaxies (LTGs) (Dressler et al. 1997; Boselli & Gavazzi 2006).

The features of galaxies in clusters are determined by a combination of the initial conditions of their formation and the interactions within the environment in which they evolve. How these two aspects impact the observed population of galaxies in clusters is hotly debated in the astrophysics community. Ram-pressure stripping of the interstellar medium (ISM) is considered as the dominant mechanism to affect the properties of galaxies in clusters (Boselli et al. 2022; Xie et al. 2025): as they travel at high velocities (up to  $\sim 1000$  km/s) through the hot and dense gas of the Intra-Cluster Medium, the ISM can be stripped away if ram-pressure overcomes the gravitational pressure anchoring the gas to the galaxy (Gunn & Gott 1972). This process is more effective for galaxies on radial orbits, which both increase their speed and bring them closer to the cluster core (Vollmer et al. 2001; Singh et al. 2019).

Moreover, Tammann (1972), Moss & Dickens (1977), Sodr  et al. (1989), Biviano et al. (1992), Colless & Dunn (1996), Adami et al. (1998), and later Boselli & Gavazzi (2006), showed that the line-of-sight (LoS hereafter) velocity distributions of galaxies in clusters is type-dependent. While ETGs display a virialised Gaussian velocity distribution, LTGs exhibit strong deviations from Gaussianity, being the distribution generally broader and, in some cases, asymmetric (Zabludoff & Franx 1993; Biviano et al. 1997). These differences in velocity distri-

\* E-mail: s.pedratti1@campus.unimib.it

\*\* Scientific associate INAF - Osservatorio Astronomico di Cagliari, Via della Scienza 5, 09047 Selargius (CA), Italy

butions are probably due to LTGs orbits being more elongated and to their anisotropic infall from the surrounding large scale filaments, and serve as an indirect evidence for their infall onto the cluster core (*e.g.* Mamon et al. 2019; Pizzuti et al. 2025). The more elongated orbits of spiral, gas-rich, star forming galaxies in dense environments suggest that these galaxies are subject to dynamic gas depletion, mainly due to ram pressure stripping, leading to star formation quenching and morphological transformations of LTGs into ETGs, eventually producing the predominant population of red quiescent systems of present day clusters.

This paper focuses on the Coma Cluster (Abell 1656), one of the most massive and well-studied galaxy clusters of the Local Universe at a redshift  $z = 0.023$  (Kang et al. 2025), whose study is favoured by its position in the sky near the Milky Way’s north pole, where contamination due to dust and gas from our galaxy’s plane is negligible. Despite early indications of the presence of subclustering (see Biviano 1998, and references therein), the Coma cluster has been considered for a long time as the prototype of an old and relaxed cluster. X-ray maps (White et al. 1993; Neumann et al. 2001), analyses of projected distribution of galaxies (Baier et al. 1990) and LoS velocity distributions (Colless & Dunn 1996) established the existence of a group centred around the massive galaxy NGC 4839, that is now understood to be on secondary infall after reaching its first orbital apocentre (*e.g.* Biviano et al. 1996; Lyskova et al. 2019; Churazov et al. 2021). In addition, a recent or ongoing merger has been identified between the main cluster and a group, partially disrupted, originally dominated by NGC 4889 or NGC 4874 (Biviano et al. 1996; Adami et al. 2005). Much more recently, Costa et al. (2025) and Kang et al. (2025) found evidence of many substructures, often overlooked because of the faint nature of the galaxies tracing them. The interactions that result from this complex configuration could be at the origin of the observed post-starburst (PSB) galaxies in the periphery of the cluster (Caldwell et al. 1993; Gavazzi et al. 2010).

After Zwicky (1933)’s first estimate of the total mass, many studies focused on getting more precise determinations of the total mass distribution through several independent measurements. More specifically, Łokas & Mamon (2003) performed a kinematic analysis of elliptical galaxies in the cluster field to obtain a total mass  $M_{200} = 1.2 \times 10^{15} M_{\odot}$ <sup>1</sup> with 30% accuracy, within a corresponding radius  $r_{200} = 2.2$  Mpc. Here and throughout the paper, we refer to  $M_{\Delta} = \Delta H^2(z)/(2G) \times r_{\Delta}^3$  as the cumulative mass enclosed in a radius  $r_{\Delta}$  of a spherical overdensity with an average density  $\Delta$  times the critical density of the Universe at the cluster redshift  $\rho_c(z)$ . Following similar prescription in the literature, we define quantities at  $\Delta = 200$  as ‘virial’ mass and radius, respectively. Weak lensing calculations allowed Gavazzi et al. (2009) to estimate  $M_{200} = 5.1_{-2.1}^{+4.3} \times 10^{14} M_{\odot}$ , while a recent paper by Cha et al. (2025) employed a deep learning approach based on convolutional neural network to mitigate the potential setbacks of traditional lensing analyses, such as noise amplification and mass-sheet degeneracy, finding the value of  $M_{200} = 7.4_{-3.1}^{+2.4} \times 10^{14} M_{\odot}$ . Mirakhor & Walker (2020) combined the electron density profile, recovered from the X-ray observations of *XMM-Newton*, and the pressure profile from the *Planck* Sunyaev–Zeldovich effect (SZ, Sunyaev & Zeldovich 1972) observations to estimate the virial mass as  $M_{200} = (8.5 \pm 0.55) \times 10^{14} M_{\odot}$ , corresponding to a radius  $r_{200} = 2.0$  Mpc. Finally, Ho et al. (2022) made use

<sup>1</sup> All quantities presented in this paper are referred to a cosmological model with  $H_0 = 70$  km s<sup>-1</sup> Mpc<sup>-1</sup>,  $\Omega_m = 0.3$ , and  $\Omega_{\Lambda} = 0.7$ .

of recently developed methodologies based on Bayesian deep learning, obtaining  $M_{200} = 1.8_{-0.53}^{+0.74} \times 10^{15} M_{\odot}$  and, even more recently, Benisty et al. (2025) employed the caustics, the virial theorem, and the Hubble-flow methods to find virial masses in the range  $[1.1 - 2.9] \times 10^{15} M_{\odot}$ .

In this work we perform a kinematic analysis of the Coma Cluster’s member galaxies, using new spectroscopic data collected from DESI (Dark Energy Spectroscopic Instrument, DESI Collaboration et al. 2025) to jointly reconstruct the mass and anisotropy profiles under the assumption that the cluster is in an equilibrium configuration. We employ the MG-MAMPOSST code of Pizzuti et al. (2021), which applies the Jeans equation to the projected positions and LoS velocity distribution of member galaxies. We study the relation between the Coma Cluster member galaxies and the global cluster environment, by tracing the behavior of the orbits for different subsamples of galaxies based on their colour (red sequence, green valley, blue cloud), further discussing the impact of systematics due to mass and anisotropy models and different sample parameters (*e.g.* projected radial ranges, choice of the centre, velocity rest frame). Our findings provide the stringent constraints on the mass distribution in Coma and on the orbits of its member galaxies to date.

The work is structured as follows: Sect. 2 describes the DESI dataset of galaxies in the Coma Cluster and the preliminary analysis performed on the spatial and velocity distribution of galaxies. In Sect. 3 we provide an overview of the MG-MAMPOSST method, employed to study the kinematics of the system, and of the various models adopted in the analysis. In Sect. 4 we show our results, further discussing the impact of systematic effects and checking the robustness of our analysis. The conclusions and final considerations are reported in Sect. 5.

## 2. Dataset and preliminary analyses

### 2.1. Dataset

Our dataset comes from the first Data Release (DR1) of DESI (DESI Collaboration et al. 2025), a highly multiplexed spectroscopic instrument mounted on the Mayall 4-meter telescope at the Kitt Peak National Observatory. The Coma cluster was targeted by Science Verification (SV) programs, aimed at obtaining a high density of cluster targets. As a result, the final target density in the area is much larger than the average of the DESI survey, providing us with more than 2,000 spectra in a DESI pointing. We removed all the spectra from non-nuclear sources or misclassified stars, through visual and kinematic inspection, respectively, thus obtaining a pure sample of nuclear spectra of galaxies. We require the objects to have at least *g*- and *r*-band magnitudes ( $m_g$  and  $m_r$ , respectively) for colour selections. We further select only galaxies with  $m_r < 19.7$  mag to ensure a high spectroscopic completeness of the photometrically selected sample. We estimate the spectroscopic completeness by selecting all the extended (galaxy-like) photometric objects brighter than the magnitude cut, deriving which fraction has available DESI spectroscopy in bins of distance from the centre of the Coma cluster, and excluding the central 100 kpc, as further discussed below. We find an overall spectroscopic completeness of 91% in our sample, with no significant radial trends.

Our final spectroscopic galaxy catalogue includes 1758 galaxies and covers the angular coordinate range (J2000)  $190^{\circ} < \text{RA} < 200^{\circ}$  and  $25^{\circ} < \text{DEC} < 31^{\circ}$ , for a total sky area of  $\sim 53$  deg<sup>2</sup> around the Coma Cluster region, extending out to  $\sim 3 r_{200}$ . We consider the cluster centre to be located at (RA =

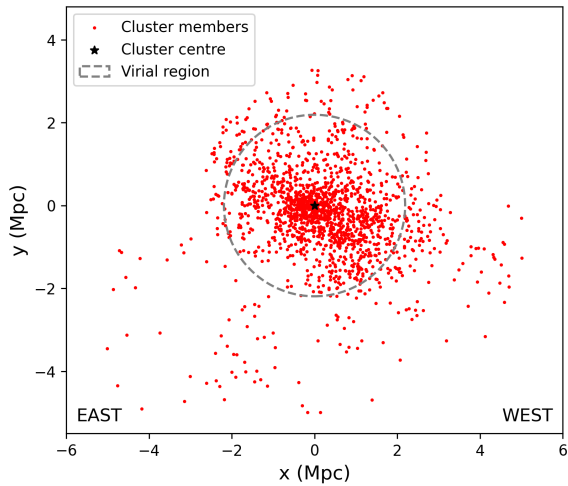


**Fig. 1.** Projected positions of galaxies in the Coma Cluster. The point marked with a black star indicates the cluster centre, whose coordinates (RA=194.90 deg, DEC=27.96 deg) have been taken from Malavasi et al. (2020) as the position of NGC 4874, while the grey circle encloses the region within  $r_{200} = 2.19$  Mpc, quoted in Boselli & Gavazzi (2006).

194.90 deg, DEC = 27.96 deg), corresponding to the position of the elliptical galaxy NGC 4874 (see *e.g.* Malavasi et al. 2020). In order to avoid systematics in the kinematic analyses, it is essential to remove the interlopers, i.e. galaxies that are within the virial radius in projection but that are outside the virial sphere. This step has been performed using the Clean algorithm (Appendix B of Mamon et al. 2013), which provides a more refined approach with respect to a simple phase-space cut. Fig. 1 depicts the projected positions of the 1651 galaxies in our final Coma Cluster sample. As we will discuss in Sect. 3, our kinematic analysis requires the projected positions  $R$  from the cluster centre and the LoS velocities of the member galaxies  $v_{\text{RF}}$ , computed in the cluster’s rest frame. The space of pairs  $(R, v_{\text{RF}})$  is called projected phase-space (p.p.s. hereafter), shown in Fig. 2.

In order to study the orbital properties of different galaxy populations, we split the sample into three main categories according to their position in the  $(m_g - m_r)$  vs stellar mass ( $M_*$ ) diagram. The stellar masses have been computed from the DESI photometry using CIGALE (Boquien et al. 2019) SPS modelling with exponentially declining SFHs, BC03 models and a Chabrier (2003) IMF. The resulting classification into red sequence (RS), green valley (GV) and blue cloud (BC) galaxies follows the representation chosen by Boselli et al. (2014) to study the Virgo cluster and is sensible to the different ages of galaxies. We start by visually identifying the RS galaxies and fitting them with a straight line; then, we assign galaxies to the GV if they lie between  $2\sigma$  and  $5\sigma$  from the RS, where  $\sigma$  is the dispersion of the RS  $(m_g - m_r)$  colours at given mass. We therefore consider as RS galaxies those with  $m_g - m_r > 0.07 \log(M_*/M_\odot) + 0.03$ , as BC galaxies those with  $m_g - m_r < 0.07 \log(M_*/M_\odot) - 0.07$ , and as GV those in between. While the  $m_g - m_r$  colour does not offer a large wavelength baseline, and the GV classification is not unique, our results are not affected by the exact choice of the GV location, given the small number of galaxies in this region. Finally, 19 galaxies are removed from the classification due to unreliable photometry. The resulting subsamples consist of 1216 RS, 167 GV, and 249 BC galaxies, for a total of 1632 galaxies, whose  $(m_g - m_r)$  vs  $M_*$  diagram is shown in Fig. 3.

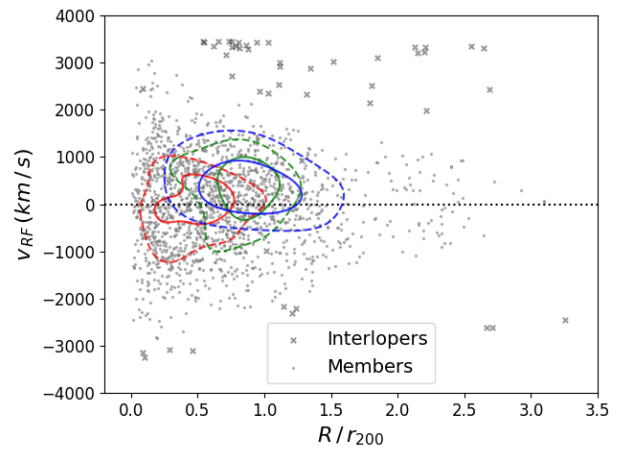


**Fig. 2.** Projected phase-space distribution of member galaxies in the Coma Cluster (grey dots) and interlopers removed by Clean (grey crosses). The black dashed line indicates the average velocity of the cluster (Hubble + bulk motion), while coloured curves highlight iso-density contours (dashed and solid lines correspond to 90th and 97th percentiles, respectively) for RS (red), GV (green) and BC (blue) galaxies. The projected distance from the centre is normalized to  $r_{200}$ , taken equal to the value quoted in Boselli & Gavazzi (2006), 2.19 Mpc

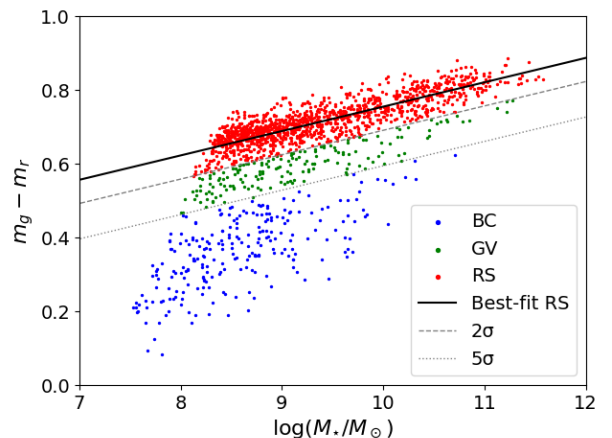


**Fig. 3.**  $(m_g - m_r)$  vs stellar mass diagram. The colour of the markers highlights the three colour classes: blue cloud (BC) in blue, red sequence (RS) in red and green valley (GV) in green. The solid line represents the best fit for RS galaxies, the dashed and dotted lines indicate the  $2\sigma$  and  $5\sigma$  limit, respectively.

## 2.2. Numerical density profile

The distribution of galaxies in clusters is shaped by that of dark matter, which dominates the total mass of the system and determines the overall gravitational potential. A widely adopted model to describe the total mass density profiles of gravitationally bound systems, such as galaxy clusters, is the Navarro-Frenk-White (NFW) model (Navarro et al. 1997):

$$\rho_{\text{NFW}}(r) = \frac{\rho_{0,\text{NFW}}}{(r/r_s)(1+r/r_s)^2}, \quad (1)$$

proportional to  $r^{-1}$  in the innermost region and to  $r^{-3}$  at large radii. In Eq. 1,  $\rho_0$  is the characteristic density of the cluster and

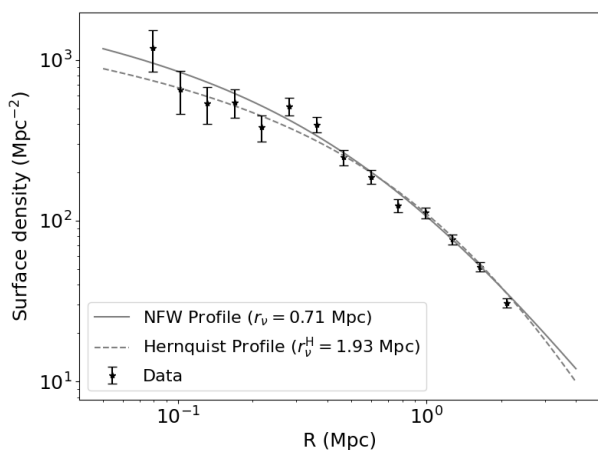


**Fig. 4.** Projected surface density profile of the Coma Cluster fitted with NFW (solid line) and Hernquist (dashed line) models. The error bars correspond to the Poisson uncertainties.

$r_s = r_{-2}$  is the scale radius at which the logarithmic derivative of the profile equals  $-2$ . While initially proposed as a description of dark matter halos in N-body cosmological simulations, the NFW profile has been shown to provide an adequate description of the total mass distribution of clusters (e.g. Umetsu et al. 2016; Pizzuti et al. 2025).

The projection of the NFW profile (Bartelmann 1996) is found to be also suitable to describe the spatial distribution of cluster members  $\nu(r)$  on the plane of the sky (e.g. Lin et al. 2004; Annunziatella et al. 2014; Sartoris et al. 2020); however, it is important to note that the scale radius of the number density of galaxies  $r_\nu$  is not in general the same as the scale radius  $r_s$  of the mass profile (Biviano & Salucci 2006; Budzynski et al. 2012). In fact, while RS galaxies typically follow a similar distribution to that of dark matter, BC galaxies tend to have a much less concentrated profile, with typical values of  $r_\nu^{\text{BC}} \sim 4 r_\nu^{\text{RS}}$  (e.g. Collister & Lahav 2005).

We further consider the Hernquist model (and its projection, Hernquist 1990), which exhibits a faster decline at large radii:

$$\nu_{\text{Her}}(r) \propto \frac{1}{(r/r_\nu^{\text{H}})(1 + r/r_\nu^{\text{H}})^3}, \quad (2)$$

with the characteristic scale  $r_\nu^{\text{H}} = 2 r_{-2}$  typically two times the corresponding scale radius  $r_\nu$  of the projected NFW model.

We fit the numerical distribution of member galaxies, required in the kinematic analysis, with both projected models – NFW and Hernquist – performing a maximum likelihood fit that does not require the binning of the data (Sarazin 1980; Biviano et al. 2013), assuming a constant completeness of the sample in the projected radial distance explored.

The best fit values obtained are  $r_\nu = 0.71^{+0.07}_{-0.06}$  Mpc in the case of NFW and  $r_\nu^{\text{H}} = 1.93^{+0.03}_{-0.46}$  Mpc with Hernquist. Both models match the observed numerical distributions adequately well, with no significant differences; as such, during the rest of this work we assume a projected Hernquist model as the reference model for the numerical distribution. The validity of this choice is assessed in Appendix A, where we compare the outcome of MG-MAMPOST runs with projected NFW and Hernquist models and we treat the scale radius  $r_\nu/r_\nu^{\text{H}}$  both as a free and fixed parameter. Fig. 4 shows the projected surface density profile of galaxies fitted with both profiles.

Since in this work we analyse different subsamples of galaxies based on their colours, we further perform a fit of the numerical profiles of RS, BC, and GV separately, assuming a Hernquist model (see the plot in Appendix B), finding the scale radii  $r_\nu^{\text{RS}} = 1.64^{+0.02}$  Mpc,  $r_\nu^{\text{BC}} = 5.82^{+3.49}_{-1.80}$  Mpc and  $r_\nu^{\text{GV}} = 12.79$  Mpc with a lower  $1\sigma$  uncertainty of 5.71 Mpc, while the upper bound remains unconstrained due to the particularly flat distribution of GV galaxies in our sample. It is worth to notice that these results are consistent with the expectation  $r_\nu^{\text{BC}} \sim 4 r_\nu^{\text{RS}}$  (e.g. Collister & Lahav 2005).

### 2.3. LoS velocity distributions

As a first diagnostic of the dynamical state of the system, we study the deviations from Gaussianity of the LoS rest-frame velocity distribution of member galaxies (Pizzuti et al. 2020). This indicator strongly correlates with other commonly used relaxation diagnostics based on X-ray observations, reinforcing its suitability for characterising the global dynamical state of a cluster (Roberts et al. 2018). As mentioned in Sect. 1, observations and simulations consistently show that in dynamically relaxed systems the distribution of LoS velocities are nearly Gaussian, whereas unrelaxed or disturbed systems exhibit significant departures from Gaussianity (Yahil & Vidal 1977; Boselli & Gavazzi 2006; Ribeiro et al. 2013). To quantify such deviations, we apply the Anderson-Darling test (Anderson & Darling 1952) on the LoS velocity distributions for RS, GV, and BC subsamples, up to 3 Mpc. Values of the Anderson-Darling distance  $A^2$  coefficient that are above 0.752 indicate a  $\geq 95\%$  confidence that the velocity distribution is inconsistent with a Gaussian.

The LoS velocity distributions for RS, GV, and BC galaxies are shown in Fig. 5. The three distributions are not significantly different, according to a Kruskal-Wallis test (Kruskal & Wallis 1952), nor are their medians, according to two-by-two comparisons by the Sign test (Dixon & Mood 1946). However, the three distributions display different shapes. The resulting  $A^2$  coefficient for RS galaxies is  $\sim 0.29$ , a low value which suggests that orbits are almost completely virialised. On the contrary, BC galaxies exhibit a notable deviation from Gaussianity with  $A^2 \sim 1.56$ , corresponding to a probability value of less than 1%, due to a skewed distribution towards higher velocities. The excess of high velocities for BC galaxies is clearly visible in Fig. 2 at  $R < r_{200}$ , and it causes a negative correlation between  $R$  and  $v_{\text{RF}}$  (Spearman rank correlation coefficient  $r = 0.097$ , corresponding to a probability of 0.05). No such correlation is present for the RS and GV classes. These characteristics of the BC velocity distribution suggest more elongated orbits for LTGs, which might be infalling towards the cluster centre from a filamentary-like structure at the near-side of the cluster along the LoS. This interesting feature will be addressed specifically in an upcoming paper (paper II), dedicated to substructures and dynamical state. GV galaxies velocity distribution shows a quite unrelaxed behaviour too, with a coefficient  $A^2 \sim 1.27$ , lower than that of the BC but significantly higher than that of the RS. As for the full sample, we found a value of  $A^2 \sim 0.80$ , higher than that of the RS but smaller than that of the GV, which indicates that the overall system is quite far from a full dynamical relaxation state, consistently with the presence of still infalling star forming galaxies.

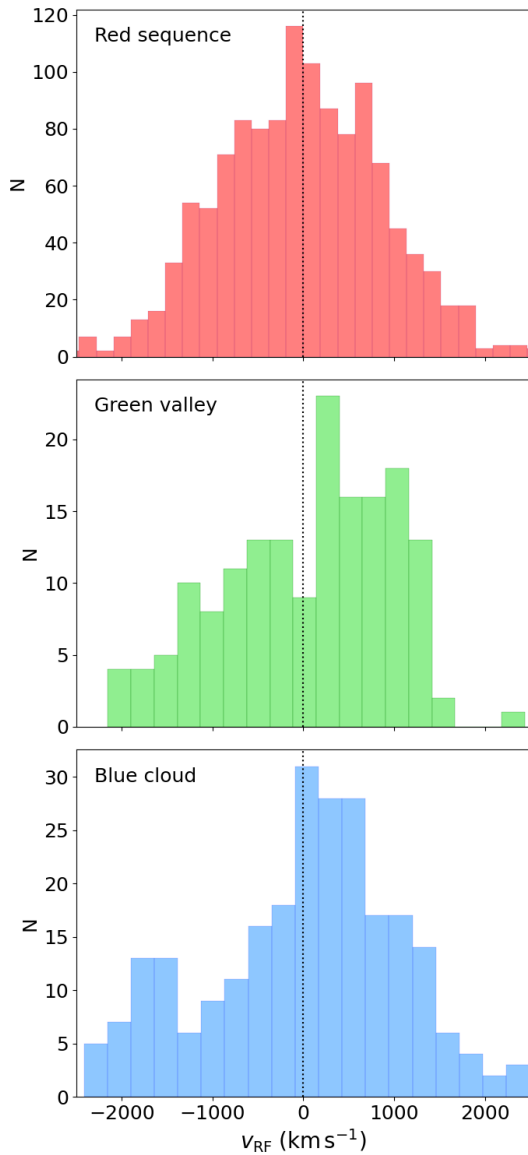


**Fig. 5.** LoS velocity distributions of RS (upper panel), GV (middle panel) and BC (lower panel) galaxies. The vertical dashed line indicates the average velocity of the cluster.

### 3. Kinematic analysis with MG-MAMPOSSt

We perform a kinematic analysis of the Coma Cluster member galaxies by means of the MG-MAMPOSSt (Modified Gravity - Modelling Anisotropy and Mass Profiles of Observed Spherical Systems) code of Pizzuti et al. (2021), an extended version of the MAMPOSSt algorithm of Mamon et al. (2013), which reconstructs galaxy cluster total mass and velocity anisotropy profiles in a wide variety of cosmological setups (including  $\Lambda$ CDM and several modified gravity/dark energy frameworks).

MAMPOSSt is a way to jointly reconstruct the anisotropy and mass profiles of spherical systems using kinematics of the system's members. In particular, the code assumes dynamical relaxation, spherical symmetry and a shape for the three-dimensional velocity distribution of the tracers of the gravitational potential (*i.e.* cluster member galaxies). Taking as input the p.p.s. dataset  $(R, v_{\text{RF}})$ , MAMPOSSt performs a Maximum Likelihood fit to solve the stationary and spherically symmetric Jeans equation:

$$\frac{d[v(r)\sigma_r^2(r)]}{dr} + 2\beta(r)\frac{v(r)\sigma_r^2(r)}{r} = -v(r)\frac{d\Phi(r)}{dr}, \quad (3)$$

where  $v(r)$  is the number density profile of galaxies,  $\sigma_r(r)$  is the velocity dispersion along the radial direction,  $\beta(r)$  is the orbital anisotropy profile and  $\Phi(r)$  is the gravitational potential, linked to the dynamical mass profile through the Poisson equation:

$$\frac{d\Phi}{dr} = \frac{GM_{\text{dyn}}(r)}{r^2}. \quad (4)$$

The orbital anisotropy profile  $\beta(r)$  is defined as:

$$\beta(r) = 1 - \frac{\sigma_\theta^2 + \sigma_\phi^2}{2\sigma_r^2}, \quad (5)$$

where  $\sigma_\theta^2$  and  $\sigma_\phi^2$  are the velocity dispersions along the tangential and azimuthal directions, respectively. This reduces to

$$\beta(r) = 1 - \frac{\sigma_\theta^2}{\sigma_r^2} \quad (6)$$

in the case that the cluster velocity structure is invariant under rotation about its center, for which  $\sigma_\theta^2 = \sigma_\phi^2$ . Negative values of  $\beta(r)$  indicate tangentially-biased orbits, while positive values signify a preference for radial orbits. A value close to  $\beta = 0$  indicates isotropic orbits, typical of central regions of dynamically relaxed systems. Previous studies based on observations (*e.g.* Host 2009; Biviano et al. 2013) and simulations (*e.g.* Hansen & Moore 2006; Mamon et al. 2010) of galaxy clusters indicate a growing trend with radius for anisotropy, from central isotropy.

MAMPOSSt estimates the probability  $q(R_i, v_i^{\text{RF}} | \theta)$  of observing the  $i$ -th tracer of the gravitational potential (*e.g.* a cluster galaxy) at a projected distance from the cluster centre ( $R_i$ ) and LoS rest-frame velocity ( $v_i^{\text{RF}}$ ), given the set of parameters  $\theta$  defining the models for  $M_{\text{dyn}}(r)$  and  $\beta(r)$ . Other similar approaches have been proposed that use additional information from the observed kinematics beyond the simple velocity dispersion profile, *e.g.* the kurtosis profile (Łokas 2002). The output of the code is the best fit estimate of the parameters  $\theta$  and the corresponding value of  $-\ln \mathcal{L}$ , computed as:

$$-\ln \mathcal{L} = - \sum_{i=1}^N \ln q(R_i, v_i^{\text{RF}} | \theta), \quad (7)$$

where  $N$  is the total number of tracers. The current implementation of MG-MAMPOSSt assumes a 3D Gaussian velocity distribution; despite its simplicity, this choice has been proven to be valid also when the LoS velocity distribution significantly deviates from Gaussianity (Mamon et al. 2013; Read et al. 2021). Refer to Mamon et al. (2013) for all the expressions regarding the MAMPOSSt procedure.

For our kinematic analysis, we consider a total sample (*i.e.* BC + RS + GV) of 1324 galaxies out of 1651 members, within a projected radius  $R \geq 0.10$  Mpc and  $R \leq 2.30$  Mpc (chosen as 1.1 times our initial guess for  $r_{200}$ ) from the cluster centre. We exclude the innermost region, as done in many similar works, where cluster dynamics is dominated by the BCG and the mass profile  $M_{\text{dyn}}(r)$  is likely to deviate from simple profiles that are known from cosmological simulations to adequately describe the

distribution of dark matter (e.g. NFW). Moreover, in Coma the core is dominated by two bright galaxies, namely NGC 4874 and NGC 4889, which would need a non-trivial modelling of the mass profile.

As for the external regions, at large radii, galaxies are likely to belong to surrounding large-scale structures (e.g. Malavasi et al. 2020), and are not gravitationally bound to the cluster, so that they cannot be used as tracers of the cluster potential in the dynamical equilibrium configuration. To ensure the robustness of the mass and anisotropy reconstruction, we performed additional runs of MG-MAMPOSS<sub>T</sub> varying the inner and outer radius, changing the centre and the velocity rest frame of the cluster. The results of these tests are reported in Sect. 4.2.

We explore four different mass models for the total mass of the Coma Cluster in the kinematic analysis. We have employed the classical NFW (see Eq. 1), whose total mass can be written as

$$M_{\text{NFW}}(r) = M_{200} \frac{\ln(1 + r/r_s) - \frac{r/r_s}{(1+r/r_s)}}{\ln(1 + c_{200}) - \frac{c_{200}}{(1+c_{200})}}, \quad (8)$$

where  $c_{200} = r_{200}/r_s$  is called ‘concentration’, together with its generalized version gNFW (Nagai et al. 2007):

$$M_{\text{gNFW}}(r) = M_{200} (r/r_{200})^{3-\alpha} \times \frac{{}_2F_1(3-\alpha, 3-\alpha, 4-\alpha, -r/r_s)}{{}_2F_1(3-\alpha, 3-\alpha, 4-\alpha, -r_{200}/r_s)}, \quad (9)$$

where  ${}_2F_1(a, b, c, x)$  is the ordinary (Gaussian) hypergeometric function (e.g. Mamon et al. 2019). This model adds an extra free parameter  $\alpha$  that controls the slope. Note that, instead of the characteristic density  $\rho_0$ , we consider the virial radius  $r_{200}$  as a free parameter of all the profiles.

The Hernquist (Hernquist 1990),

$$M_{\text{Her}}(r) = M_{200} \frac{(r_{200} + r_{\text{H}})^2}{r_{200}^2} \frac{r^2}{(r + r_{\text{H}})^2}, \quad (10)$$

and the Burkert (Burkert 1995) models:

$$M_{\text{Bur}}(r) = M_{200} \frac{\ln[1 + (r/r_{\text{B}})^2] + 2 \ln(1 + r/r_{\text{B}}) - 2 \arctan(r/r_{\text{B}})}{\ln[1 + (c_{\text{B}})^2] + 2 \ln(1 + c_{\text{B}}) - 2 \arctan(c_{\text{B}})}, \quad (11)$$

have been further adopted in the analysis. In eq. (10),  $r_{\text{H}} = 2r_{-2}$ , while in eq. (11),  $r_{\text{B}} \simeq 0.657r_{-2}$  and  $c_{\text{B}} = r_{200}/r_{\text{B}}$ . The Burkert profile has the same asymptotic behaviour as NFW but exhibits a core in the centre ( $\rho \propto \text{const}$ ) rather than a cusp, and a sharper transition from slope 0 to slope 3 than NFW. We will denote with  $r_{\rho}$  the general scale radius, which takes the form of  $r_s$ ,  $r_{\text{H}}$  or  $r_{\text{B}}$  depending on the mass model used.

For the anisotropy profile, we consider two general models, namely a generalized version of the Tiret et al. (2007, gT, hereafter) profile,

$$\beta_{\text{gT}}(r) = \beta_0 + (\beta_{\infty} - \beta_0) \frac{r}{r + r_{\beta}}, \quad (12)$$

and the generalized Osipkov-Merritt model (Osipkov 1979; Merritt 1985) (gOM),

$$\beta_{\text{gOM}}(r) = \beta_0 + (\beta_{\infty} - \beta_0) \frac{r^2}{r^2 + r_{\beta}^2}. \quad (13)$$

where  $\beta_0$  and  $\beta_{\infty}$  are the anisotropies at the centre and large radii, respectively, and  $r_{\beta}$  is a characteristic radius. These profiles capture a large variety of orbits from the innermost region to the outskirts of a cluster. Note that, as done in previous works (e.g. Mamon et al. 2019; Biviano et al. 2024), we assume  $r_{\beta} = r_{-2}$  of the mass profile, a reasonable assumption to avoid an extra free parameter in the fit, which, in our case, would be largely unconstrained.

The high-quality performances of the DESI instrument results in very small uncertainties on the LoS velocities (see DESI Collaboration et al. 2025), which are  $< 10$  km/s for emission line galaxies and between 5-30 km/s for passive galaxies, as a function of magnitude. As such, in our analysis we adopt a constant uncertainty of  $40 \text{ km s}^{-1}$ , as a conservative safe upper limit for all the galaxies in our sample.

MG-MAMPOSS<sub>T</sub> is equipped with a Monte Carlo-Markov Chain (MCMC) module to efficiently explore the parameter space, based on a simple Metropolis-Hastings algorithm with a fixed-step Gaussian random walk; the code can handle both flat and Gaussian priors on the free parameters. In the following, we sample 110000 points and discard the first 10000 as burn-in phase. This number of steps is sufficient to ensure the convergence of the chains; checks has been performed by previous studies in similar frameworks (Pizzuti et al. 2024; Biviano et al. 2025), where the Gelman-Rubin diagnostic coefficients  $\hat{R}$  (Gelman & Rubin 1992) have been computed after performing 5 chains on each run, satisfying the requirement of  $\hat{R} < 1.1$ . Each chain takes  $\lesssim 1$  hour to be completed. The details of the analysis and the results of MG-MAMPOSS<sub>T</sub> on the various subsamples of member galaxies are presented and discussed in the next Section.

## 4. Results & Discussion

### 4.1. Mass and anisotropy profiles analysis

The strategy we adopted to robustly model the mass and orbital anisotropy profiles of the Coma Cluster is the following: first, we performed a run of MG-MAMPOSS<sub>T</sub> on the p.p.s. of the mixed sample of 1324 galaxies, thus using all the RS, GV, and BC populations as tracers of the gravitational potential. This methodology has been used several times in the literature and it has been shown to work quite well when comparing to independent mass estimates (e.g. Sartoris et al. 2020; Biviano et al. 2013, 2023b). Then, we split the sample by colour class and we ran MG-MAMPOSS<sub>T</sub> separately on each population to infer the mass profiles predicted by RS, GV, and BC galaxies, respectively. The colour-dependent posterior distributions of the mass profile parameters were then combined to get the final constraints on the cluster mass profile. This procedure allowed us to check whether the two independent Bayesian estimates are in agreement within each other, and provide further support to the viability of mixing different galaxy populations to reconstruct the total gravitational potential of clusters.

We considered two free parameters for the mass profile,  $r_{200}$  and  $r_{\rho}$  – in the case of NFW, Burkert and Hernquist models. We also treated the scale radius of the numerical density profile  $r_{\nu}^H$  as a free parameter, assuming a projected Hernquist model (see Appendix A). In addition, letting  $\mathcal{A} = \sigma_r/\sigma_{\theta} = (1 - \beta)^{-1/2}$ , we adopted two free parameters for the velocity anisotropy:  $\mathcal{A}_0$  and  $\mathcal{A}_{\infty}$  for the inner and outer values, respectively. This definition rescales the range  $-\infty < \beta < 1$  into  $0 < \mathcal{A} < \infty$ , preventing numerical issues at  $\beta \sim 1$ . For the gNFW model, the

**Table 1.** Assumed priors for MG-MAMPOST runs with mixed components.

Parameter	Prior type	Min	Max
$r_{200}$ (Mpc)	log-Flat	$\log_{10}(1.0/\text{Mpc})$	$\log_{10}(3.0/\text{Mpc})$
$r_p$ (Mpc)	log-Flat	$\log_{10}(0.2/\text{Mpc})$	$\log_{10}(5.0/\text{Mpc})$
$r_v^H$ (Mpc)	log-Flat	$\log_{10}(1.4/\text{Mpc})$	$\log_{10}(2.1/\text{Mpc})$
$\mathcal{A}_0$	Flat	0.5	5.0
$\mathcal{A}_\infty$	Flat	0.5	5.0
$\alpha$	Flat	0.1	1.9

**Notes.**  $\alpha$  is a free parameter only when the gNFW model is used for the mass density profile.

additional exponent  $\alpha$  was further optimized within the fit. The assumed priors are listed in Table 1: they are flat for every parameter and uninformative for each of them except for  $r_v^H$ , for which we adopted informative priors based on the best fit values discussed in Sect. 2.2.

Different combinations of  $M_{\text{dyn}}(r)$  and  $\beta(r)$  models provided mass estimates in agreement within the uncertainties, which indicates robustness of the results. Since some runs involved a different number of galaxies or free parameters, we used the Bayesian Information Criterion (BIC) and the Akaike Information Criterion (AIC) to provide a rough estimate of the performance of each combination of models. The BIC criterion is defined as:

$$\text{BIC} = k \ln(N) - 2 \ln \mathcal{L}, \quad (14)$$

where  $k$  is the number of free parameters in the run,  $N$  is the total number of tracers used in the analysis, in our case the member galaxies, and  $\ln \mathcal{L}$  is the best fit log-likelihood. Lower BIC values indicate preferred models: in fact, the penalty term  $k \ln(N)$  increases with both the number of parameters and the number of data points, discouraging overly complex models unless they provide a significantly better fit. As  $k$  increases, the model gains flexibility and typically achieves a higher (less negative) log-likelihood, but this comes at the cost of a larger penalty. Conversely, a model with fewer free parameters is rewarded by a smaller penalty. Similarly, the AIC criterion is defined as:

$$\text{AIC} = 2k - 2 \ln \mathcal{L}, \quad (15)$$

which, in our case, reduces the penalty caused by the increasing of the number of free parameters. In this analysis, only the runs assuming a gNFW model for the mass density profile present an extra free parameter; therefore, a comparison of the BIC/AIC parameter between runs not using gNFW and considering the same number of galaxies in the analysis essentially consists in checking the difference in the respective log-likelihoods.

The resulting BIC and AIC values suggest that the NFW model for the mass profile is favoured with respect to the Burkert and Hernquist models, and the gOM anisotropy model is slightly better than the gT model, but differences in the Bayesian evidence values are negligible. Therefore, we considered as the reference estimates for the parameters with mixed components those of the NFW gOM run, reported in the corresponding column of Table 2. Note that the best fit values reported in every Table of this paper correspond to the maximum likelihood values.

For the mixed-population run, we plot the reconstructed mass profile along with its  $1 \sigma$  and  $2 \sigma$  uncertainty regions as the

purple dashed and dotted lines, respectively, in Fig. 6 (left panel). The anisotropy profile, shown in Fig. 7, indicates the presence of radial orbits both in the outer and in the inner regions of the system, with only a slight variation with radius. The prevalence of radial orbits reflects the presence of a population of recently accreted galaxies from the surrounding large-scale structure.

It is worth to point out that our constraints on  $r_s$  are consistent with the concentration values found by Gavazzi et al. (2009). When running with the gNFW, the inner slope of the mass density profile is estimated as  $\alpha = 1.71^{+0.16}_{-0.39}$ , at the cost of a totally unconstrained scale radius of the mass profile. The BIC for this run is 7 units higher (worse) than the reference run, but the difference reduces to only 2 units when using the AIC criterion.

We then ran MG-MAMPOST on the p.p.s. of the different colour classes. Based on the analysis performed with the mixed components, here we kept the NFW and the gOM as the reference mass density and anisotropy profile models. The employed priors were the same as those used for the mixed sample analysis (Table 1), with the exception of  $r_v^H$  for which priors were adapted for each class following the results of Sect. 2.2. The number of galaxies between 0.10 Mpc and 2.30 Mpc – the minimum and maximum radii considered for the reference analysis – is 1030 for the RS, 129 for the GV, and 152 for the BC. The estimates of the free parameters, for each of the three populations, are reported in the corresponding columns of Table 2.

As expected, the dynamics is completely dominated by the RS galaxies, producing a profile in excellent agreement with that obtained from the mixed sample, as further shown by the red solid curve in Fig. 6 (left). While the analysis of the GV sample tends to underestimate the total mass at all radii, the BC galaxies favour a less concentrated and more massive cluster, supporting the idea that they are farther away from dynamical equilibrium.

When combining the three marginalised posterior distributions  $\ln P_{\text{joint}}(r_{200}, r_s) = \sum_i P_i(r_{200}, r_s)$ , with  $i = \text{RS, BC, GV}$ , we obtain  $M_{200} = 1.08^{+0.08}_{-0.09} (\text{stat}) \pm 0.09 (\text{syst}) \times 10^{15} M_\odot$ , corresponding to  $r_{200} = 2.12 \pm 0.06 (\text{stat}) \pm 0.07 (\text{syst}) \text{ Mpc}$  and a scale radius for the mass profile  $r_s = 0.48^{+0.27}_{-0.13} \text{ Mpc}$ . The systematic uncertainties take into account the variation of the best fit due to different choices of the mass and anisotropy models, as well as the variations of projected radial range considered, cluster centre and velocity rest frame (see Sect. 4.2). The mass profile and the corresponding  $1$  and  $2 \sigma$  regions are shown as grey shaded areas in the left panel of Fig. 6 (left). The right panel of the same Figure displays the relative ratio between ours and other estimates from the literature for the total mass profile of the cluster. Overall, we found a general good agreement among different mass profiles within uncertainties, with the largest deviations found near the centre. The weak lensing analysis of Gavazzi et al. (2009) predicts a lower cluster mass, but still in agreement with our value within the  $1 \sigma$  region. For a comparison between our best virial mass measurement and those coming from more recent studies, see also Fig. 11 and the discussion in Sect. 5.

Finally, we performed an additional run to estimate the diffuse dark matter mass profile of the cluster at  $r > 0.10 \text{ Mpc}$ . We considered the total (spherical) gas mass  $M_{\text{gas}}(r)$  estimated from the electron density profile (Mirakhor & Walker 2020) and the total stellar mass in galaxies. From the cumulative projected stellar mass distribution  $M_*(R)$  we obtained the three-dimensional stellar mass profile by fitting a Hernquist model, similarly to what done for the number density distribution, and assigning weights to each galaxy proportional to their mass.

**Table 2.** Best fit parameters for the runs with mixed and separated components.

Parameter	Mixed	RS	GV	BC	Joint
$r_{200}$ (Mpc)	$2.14^{+0.09}_{-0.05}$	$2.06^{+0.07}_{-0.05}$	$1.57^{+0.48}_{-0.18}$	$2.55^{+0.21}_{-0.44}$	$2.12 \pm 0.06$
$r_s$ (Mpc)	$0.70^{+0.22}_{-0.30}$	$0.61^{+0.02}_{-0.37}$	$0.83^{+0.85}_{-0.62}$	$2.42^{+0.05}_{-2.18}$	$0.48^{+0.27}_{-0.13}$
$r_v^H$ (Mpc)	$1.70^{+0.11}_{-0.13}$	$1.27^{+0.12}_{-0.08}$	$7.40^{+2.60}_{-2.48}$	$5.17^{+1.32}_{-1.72}$	/
$\mathcal{A}_0$	$1.10^{+0.65}_{-0.33}$	$1.00^{+0.68}_{-0.30}$	$0.81^{+1.22}_{-0.25}$	$1.78^{+0.79}_{-0.86}$	/
$\mathcal{A}_\infty$	$1.46^{+0.20}_{-0.58}$	$1.60^{+0.02}_{-0.58}$	$1.89^{+1.44}_{-0.73}$	$0.99^{+0.78}_{-0.29}$	/

**Notes.** The employed mass and anisotropy models are NFW and gOM, respectively. The assumed priors, for these runs, are broad and flat, except for  $r_v^H$ , for which we considered informative priors based on the best fit values discussed in Sect. 2.2.

The MG-MAMPOSS<sub>T</sub> code was then applied to fit a multi-component mass model as

$$M_{\text{tot}}(r) = M_{\text{gas}}(r) + M_*(r) + M_{\text{DM}}(r), \quad (16)$$

where  $M_{\text{DM}}(r)$  is the DM distribution, parametrised as a gNFW model. The uncertainties on the stellar mass profile in galaxies and on the gas mass profile were accounted by first maximum-likelihood-fitting a Hernquist model and a  $\beta$ -model to the galaxies and gas data, respectively, and using the resulting covariance matrix as a multi-variate Gaussian input prior on the corresponding  $M_*(r)$ ,  $M_{\text{gas}}(r)$  in the MG-MAMPOSS<sub>T</sub> analysis.

The resulting mass profiles are shown in Fig. C.1 of Appendix C. The dark matter dominates at all radii, with a corresponding virial mass  $M_{200}^{\text{DM}} = 8.6_{-0.8}^{+1.2} \times 10^{14} M_\odot$ . The total mass at  $r = 2.12$  Mpc, our best fit value for the virial radius, is found to be  $M_{\text{tot}} = M_{\text{DM}} + M_{\text{gas}} + M_* = (1.09 \pm 0.10) \times 10^{15} M_\odot$  in excellent agreement with the single-profile estimates. With this multicomponent approach we can further estimate the value of the baryon fraction as  $f_b \equiv 1 - M_{\text{DM}}/M_{\text{tot}} = 0.15 \pm 0.02$  at  $r = 2.12$  Mpc, consistent with the cosmological value of  $\Omega_b/\Omega_m$  (e.g. Krolewski & Percival 2025).

#### 4.2. Robustness of mass-orbital modelling

The MG-MAMPOSS<sub>T</sub> procedure of modelling the mass and orbital profiles of complex systems such as the Coma Cluster produces results that are inevitably depending on several choices and assumptions, whose validity and robustness must therefore be assessed. First of all, one has to assemble the input p.p.s. sample of member galaxies, which, even after the removal of interlopers, is dependent on two main variables:

- i) The coordinate centre of the cluster, which we located at (RA=194.90 deg, DEC = 27.96 deg), the position of NGC 4874.
- ii) The LoS velocity of the rest frame of the cluster, chosen as the biweight mean LoS velocity of its members.

The input parametrisations of the mass and anisotropy profiles (see Sect. 4.1), as well as for the numerical density profile (see Sect. 2.2 and Appendix A), with their relative priors choice, introduce additional potential sources of uncertainty.

The projected radial range within which galaxies are considered in the fit plays a fundamental role. This depends on:

- iii) the minimum projected radius, which we chose to be 100 kpc, in order to exclude the innermost region where dynamics is dominated by NGC 4874 and NGC 4889.
- iv) the maximum projected radius, which we chose to be 2.30 Mpc, in order to exclude the outer regions, where we cannot ensure dynamical equilibrium.

In this Section we want to verify that reasonable variations of the choices of i)–iv) lead to results that are within the uncertainties of our reference analysis of Sect. 4.1. We therefore ran MG-MAMPOSS<sub>T</sub> again to perform the following tests:

- i) We moved the coordinate centre of the cluster to the position of NGC 4889 (RA=195.03 deg, DEC=27.98 deg) and to the position of the X-ray peak of emission (RA=194.94 deg, DEC=27.95 deg) (Sato et al. 2011).
- ii) We shifted the LoS velocity of the rest frame of the cluster to the average LoS velocity of RS (which is lower by  $\sim 20$  km/s), GV, or BC galaxies (which is higher by  $\sim 53$  and  $\sim 4$  km/s, respectively).
- iii) We changed the minimum projected radius to both 50 kpc and 200 kpc.
- iv) We changed the maximum projected radius to 1.8 Mpc, 2.6 Mpc and 2.9 Mpc.

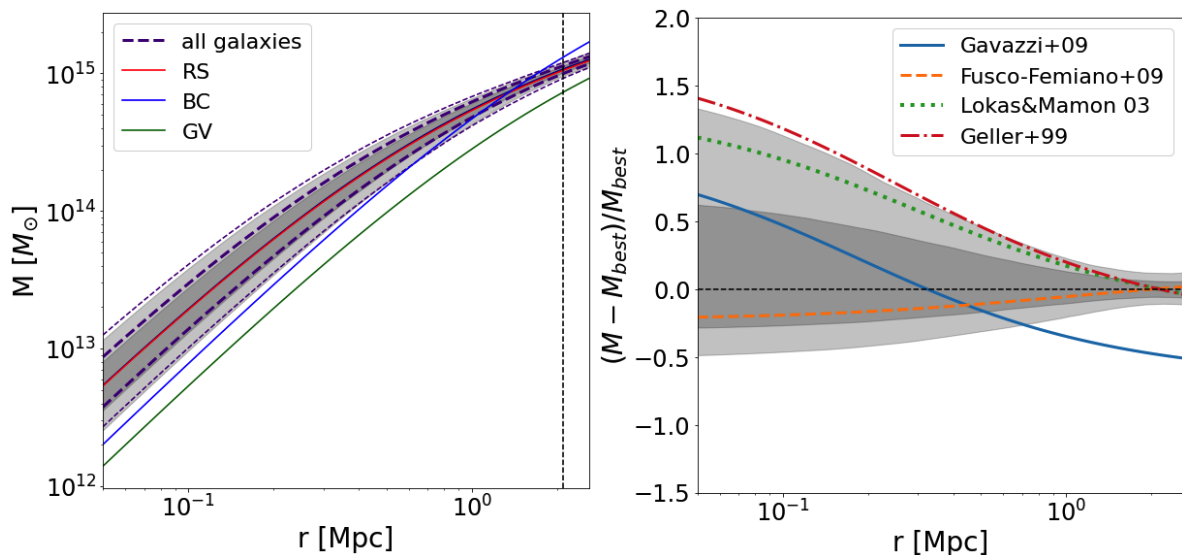
For these runs we used the same priors of Table 1 to not introduce other differences that could invalidate the tests. The comparison of the best fit estimates of  $r_{200}$  and  $r_s$  is shown in Fig. 8. All the results are fully in agreement with each other: the largest differences for  $r_{200}$  are observed when changing the maximum radius considered, producing a variation of  $\sim 5\%$  and for  $r_s$  when shifting to the GV rest frame, causing a  $\sim 30\%$  variation of the best fit, still well within the much larger uncertainties of  $r_s$  with respect to  $r_{200}$ .

Fig. 9 shows the relative variation of the anisotropy profiles produced by these runs with respect to the reference profile of Fig. 7: all the profiles are well within the  $1\sigma$  uncertainty regions of the reference run. We therefore conclude that the mass-orbital modelling of Coma with MG-MAMPOSS<sub>T</sub> is very robust and only slightly affected by systematics.

#### 4.3. Orbital anisotropy study for different colour classes

We devote this Section to the comparison of the anisotropy profiles of RS, GV, and BC galaxies. In fact, even if the profile obtained with the mixed sample does not show significant trends with radius (Fig. 7), it might be that different populations contribute differently to the orbital properties of the cluster.

In general, given the evolutionary picture of galaxies in clusters described in Sect. 1, we would expect to observe a higher value of the anisotropy for BC and GV with respect to RS galaxies. However, the runs performed in Sect. 4.1 for the different colour classes cannot be used to directly compare the anisotropy profiles, because the corresponding mass parameters are significantly different. While the values of  $r_s$  obtained from the different tracers are mutually consistent (note that the BC estimate presents very high uncertainties), this is not the case for  $r_{200}$ , for



**Fig. 6.** *Left:* Estimated mass profiles in the MG-MAMPOSS<sub>T</sub> runs for the mixed components (1 and  $2\sigma$  regions delimited by purple dashed lines), separated colour classes (RS in red, GV in green, BC in blue) and produced by the joint likelihood (1 and  $2\sigma$  regions coloured in dark and light grey, respectively, and vertical dashed line corresponding to the virial radius). *Right:* Relative ratio between our best fit  $M_{best}(r)$  and other estimates of the full mass profile of Coma from the literature. Blue solid curve: Gavazzi et al. (2009) (from weak lensing analyses). Orange dashed line: Fusco-Femiano et al. (2009) (from an X-ray data). Green dotted line: Łokas & Mamon (2003), and red dot-dashed curve: Geller et al. (1999) (both from kinematics analyses). Dark and light grey shadings indicate 1 and  $2\sigma$  confidence regions on our best fit  $M_{best}(r)$ . Confidence regions on the literature  $M(r)$  are not shown for the sake of clarity.

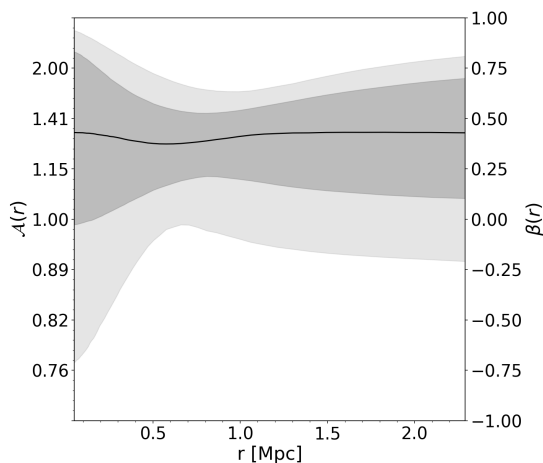


**Fig. 7.** Estimated anisotropy profile in the MG-MAMPOSS<sub>T</sub> run for the mixed components with the NFW mass model and gOM anisotropy model. The solid curve is the median profile of the MCMC chain.

which the GV estimate is lower and the BC one is higher than that of the RS. This BC result supports the hypothesis proposed in Sect. 2.3, namely that a substantial fraction of BC galaxies belongs to a filamentary-like structure along the LoS, leading to an overestimation of the cluster’s virial radius. In order to directly compare the anisotropy profiles of the populations, we need their mass parameters to be consistent a priori; therefore, we performed additional MG-MAMPOSS<sub>T</sub> runs employing Gaussian priors on  $r_{200}$  and  $r_s$  coming from the joint likelihood estimates of Sect. 4.1, obtained combining the RS, GV, and BC runs. The corresponding new results for all parameters and populations are reported in Table 3.

**Table 3.** Same as Table 2, but for the runs with Gaussian priors on  $r_{200}$  and  $r_s$  from the joint likelihood.

Parameter	RS	GV	BC
$r_{200}$ (Mpc)	$2.10^{+0.04}_{-0.05}$	$2.08^{+0.08}_{-0.03}$	$2.16^{+0.05}_{-0.06}$
$r_s$ (Mpc)	$0.58^{+0.03}_{-0.25}$	$0.57^{+0.06}_{-0.32}$	$0.74^{+0.06}_{-0.28}$
$r_v^H$ (Mpc)	$1.27^{+0.10}_{-0.08}$	$7.78^{+0.75}_{-3.48}$	$6.62^{+1.76}_{-1.52}$
$\mathcal{A}_0$	$1.20^{+0.47}_{-0.46}$	$1.76^{+1.71}_{-0.95}$	$1.37^{+1.08}_{-0.40}$
$\mathcal{A}_\infty$	$1.50^{+0.07}_{-0.40}$	$1.24^{+0.40}_{-0.38}$	$1.62^{+0.60}_{-0.40}$

**Notes.** Gaussian priors on  $r_v^H$  are based on the estimates of Sect. 2.2, while those for  $\mathcal{A}_0$  and  $\mathcal{A}_\infty$  are flat (same as Table 1).

The obtained anisotropy profiles of the different populations are shown for RS, GV, and BC galaxies in Fig. 10. By also comparing these plots with Fig. 7, relative to the profile obtained with the mixed sample, we note that all the profiles are similar within the uncertainties, with broader 1 and  $2\sigma$  regions in the centre (within  $R \lesssim 1.0$  Mpc) with respect to the outskirts. However, some differences in the median profiles are observed: in particular, the behaviour of RS galaxies is very similar to that of the mixed sample, showing a general tendency towards radial orbits both in the central regions and in the outskirts. BC galaxies, on the other hand, display even more radial orbits in the outskirts, while remaining similar to the RS population in the core. Finally, GV galaxies exhibit a strong increase in radial anisotropy in the central region, whereas their outer orbits remain comparable to those of RS galaxies. These results are consistent with a scenario in which young, star forming galaxies fall into the cluster from the outer regions and transition to the GV phase as they approach the cluster core, likely as a consequence of substantial ram-pressure stripping. This evolutionary pathway could be in-

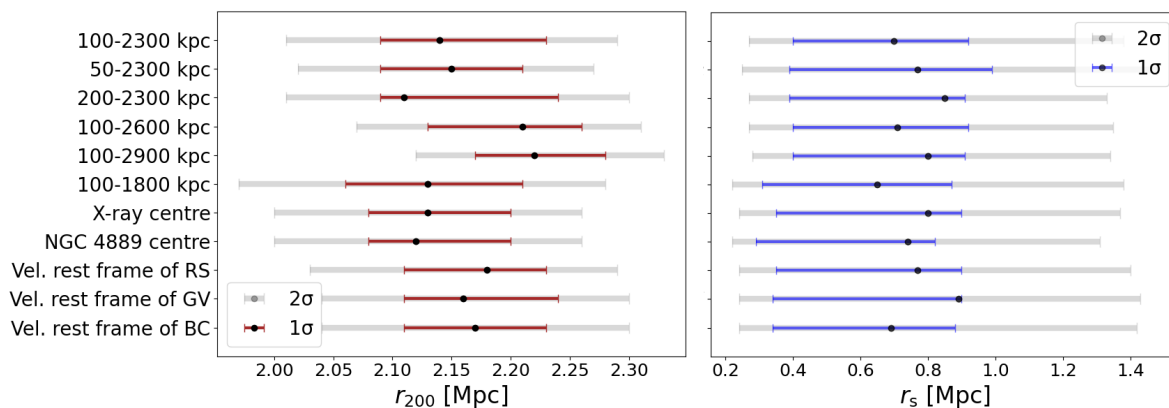


**Fig. 8.**  $r_{200}$  (left) and  $r_s$  (right) estimates and confidence intervals (1 and  $2\sigma$ ) for the different runs, specified on the left, performed to check the robustness of the mass modelling.

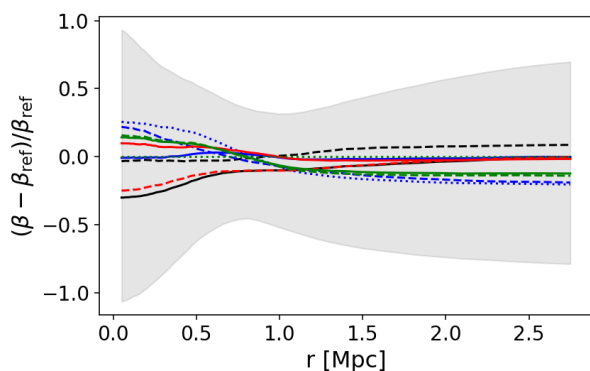


**Fig. 9.** Relative variation of the anisotropy profiles with respect to the reference profile ( $\beta_{\text{ref}}$ ) of Fig. 7 after: changing minimum radius (black) to 50 kpc (solid) and 200 kpc (dashed); changing maximum radius (blue) to 1.8 Mpc (solid), 2.6 Mpc (dashed) and 2.9 Mpc (dotted); moving the cluster centre (red) to the coordinates of NGC 4889 (solid) and of the X-ray peak (dashed); shifting the velocity rest frame (green) to that of RS (solid), BC (dashed) and GV (dotted) galaxies. The grey band identifies the  $1\sigma$  uncertainty band of the reference profile.

investigated splitting the sample in other subclasses (e.g. from the Star Formation Rate (SFR) vs  $M_*$  diagram) but we do not expect significant differences in the results. As a simple test, we split the full sample of galaxies into two equal population stellar mass bins and performed the same MG-MAMPOSS $\tau$  analysis as that for the three colour classes. The results are reported in Appendix D.

## 5. Conclusions

In this work, we performed a detailed kinematic analysis of the Coma Cluster using a novel rich spectroscopic catalogue of cluster members from the DESI survey. We applied the MG-MAMPOSS $\tau$  code to a sample of 1324 member galaxies in the projected phase space ( $R, v_{\text{RF}}$ ) up to  $R \sim 2.3$  Mpc, in order to jointly reconstruct the mass and orbital anisotropy profiles of Coma. By working with different subsamples of member galaxies, selected based on their colour, we obtained useful insights

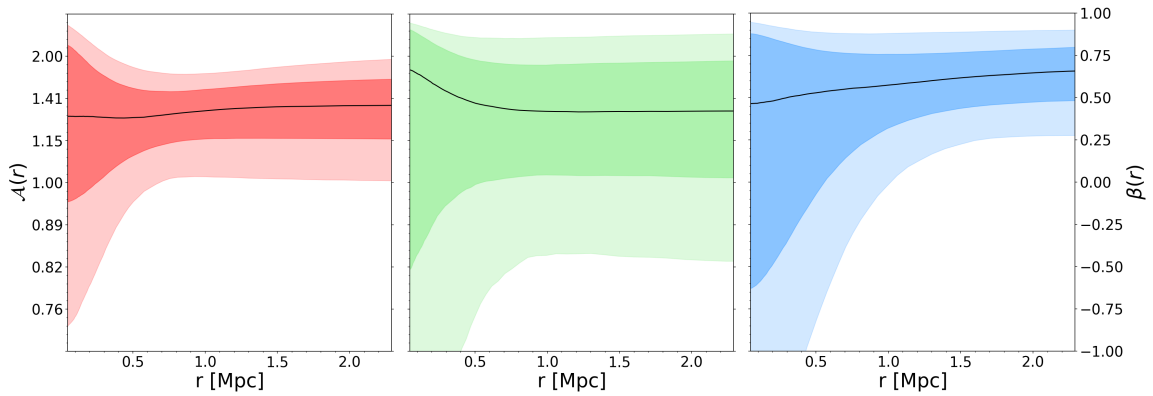
about the effect of the internal cluster dynamics on the properties of member galaxies.

We found that blue cloud (BC) galaxies, contrary to red sequence (RS) galaxies, exhibit strong deviations from Gaussianity in their LoS velocity distribution. This behaviour is consistent with theoretical predictions about LTGs still infalling towards the cluster centre, along more elongated orbits, in which the efficiency of ram-pressure stripping is higher in quenching star formation, thereby contributing to their eventual transition into ETGs.

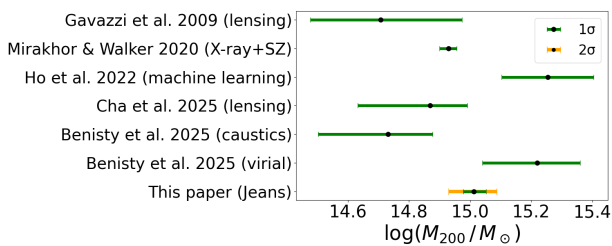
We ran MG-MAMPOSS $\tau$  on the full sample of member galaxies and on different colour subsamples, exploring various combinations of mass and anisotropy models. While all the models provide adequate fits of the total mass distribution, the NFW profile with gOM anisotropy gives the lowest BIC/AIC; we quote the Coma Cluster's virial mass, obtained from the joint likelihood of the different populations, to be  $M_{200} = 1.08^{+0.08}_{-0.09}$  (stat)  $\pm 0.09$  (syst)  $\times 10^{15} M_{\odot}$ , corresponding to  $r_{200} = 2.12 \pm 0.06$  (stat)  $\pm 0.07$  (syst) Mpc, where the systematic uncertainties account for the variation in the mode of the distribution among the combination of models and configurations tested, and the scale radius of the mass profile to be  $r_s = 0.48^{+0.27}_{-0.13}$  Mpc. When separately including the gas and stellar mass in galaxies in the fit, we estimate a dark matter virial mass  $M_{200}^{\text{DM}} = 8.6^{+1.2}_{-0.8} \times 10^{14} M_{\odot}$  and a baryon fraction  $f_b = 0.15 \pm 0.02$  at  $r = 2.12$  Mpc, in agreement with current cosmological studies.

Fig. 11 shows a graphic comparison between our  $M_{200}$  estimate and those from recent studies, in which different techniques have been adopted: weak lensing analysis, combination of X-ray and SZ effect, machine learning, caustics, and virial theorem methods. Interestingly, our best-fit value lies above the masses derived from lensing (Gavazzi et al. 2009; Cha et al. 2025), X-ray+SZ (Mirakhor & Walker 2020) and caustics methods (Benisty et al. 2025) but below the ones inferred from machine-learning (Ho et al. 2022) and virial theorem methods (Benisty et al. 2025). The  $2\sigma$  error bars of our measurement overlap with  $1\sigma$  error bars of lensing, X-ray+SZ, and virial theorem estimates, while approaching, but not reaching, the  $1\sigma$  error bars from machine learning and caustics.

The anisotropy profile shows a tendency to radial orbits both in the centre and in the outskirts, similarly to the profile obtained by Pizzuti et al. (2025) for the cluster PSZ2 G067.17+67.46. The average  $\beta(r)$  found by Biviano et al. (2025) analysing nine massive clusters from the CLASH-VLT dataset shows a similar



**Fig. 10.** Estimated anisotropy profiles in NFW gOM runs with Gaussian priors on the mass (coming from the joint results of Sect. 4.1) for RS (left), GV (middle), and BC (right) galaxies, separately. The coloured and shaded regions indicate  $1\sigma$  and  $2\sigma$  confidence intervals, respectively. Solid curves are the median profiles of each MCMC chain.



**Fig. 11.** Comparison between  $M_{200}$  estimates from different studies (indicated on the left of the figure) and our best estimate from MG-MAMPOSS<sub>r</sub> with DESI dataset.

*Acknowledgements.* LP acknowledges support by the Italian Ministry for Research and University (MUR) under 457 Grant “Progetto Dipartimenti di Eccellenza 2023-2027” (BiCoQ). LP and AR acknowledge the usage of INAF-OATs IT framework (Taffoni et al. 2020; Bertocco et al. 2020). AR acknowledges EuroHPC Joint Undertaking for awarding the project ID EHPC-REG-2024R01-029 access to Leonardo at CINECA, Italy. AR acknowledges ISCRA for awarding this project access to the LEONARDO supercomputer, owned by the EuroHPC Joint Undertaking, hosted by CINECA, Italy (HP10BUFI59).

trend, with a slightly more isotropic behaviour in the centre, as well as the orbits found for ram pressure stripped member galaxies in nearby clusters (Biviano et al. 2024). The parameter’s behaviour remains comparable between RS, GV, and BC galaxies; however, the median profiles of GV and BC galaxies show even more substantial radial tendencies in the centre and in the outskirts, respectively, while RS galaxies produce a similar profile to the mixed sample. These results are consistent with many previous anisotropy studies of different galaxy populations, which report no significant differences between the orbits of passive and star forming galaxies in clusters (*e.g.* Hwang & Lee 2008; Biviano et al. 2013). The more radial behaviour of blue galaxies in the outer regions with respect to the red ones is consistent with the outcome of Mamon et al. (2019) analyses (see *e.g.* Fig. 7) of stacked clusters from WINGS. Also, our virial mass estimates significantly differ depending on the employed tracers, with BC galaxies producing a quite larger value; this may be an indication of a filamentary-like structure along the LoS, which we will deeply investigate in the upcoming paper II. The new study will focus on the substructure content of the Coma Cluster, the possibility of a recent major merging (see Biviano et al. 1996) and the implication of the dynamical state in the mass-orbit modelling.

In summary, this work provides an important example of how studying galaxy clusters properties through a kinematic approach is a very useful strategy to constrain different scenarios of galaxy evolution. With the advent of new wide-field spectroscopic surveys, providing larger and more complete samples of galaxies in clusters, this approach will allow increasingly detailed and statistically robust studies of cluster dynamics and galaxy accretion, thereby offering new insights into the role of environment in shaping galaxy properties.

## References

- Adami, C., Biviano, A., & Mazure, A. 1998, *A&A*, 331, 439
- Adami, C., Biviano, A., Durret, F., & Mazure, A. 2005, *A&A*, 443, 17
- Anderson, T. W. & Darling, D. A. 1952, *Ann. Math. Stat.*, 23, 193
- Annunziatella, M., Biviano, A., Mercurio, A., et al. 2014, *A&A*, 571, A80
- Baier, F. W., Fritze, K., & Tiersch, H. 1990, *Astron. Nachr.*, 311, 89
- Bartelmann, M. 1996, *A&A*, 313, 697
- Benisty, D., Wagner, J., Haridasu, S., & Salucci, P. 2025, arXiv e-prints, arXiv:2504.04135
- Bertocco, S., Goz, D., Tornatore, L., et al. 2020, in *ASP Conf. Ser.*, ed. R. Pizzo, E. R. Deul, J. D. Mol, J. de Plaa, & H. Verkouter, Vol. 527, 303
- Biviano, A. 1998, in *Untangling Coma Berenices: A New Vision of an Old Cluster*, ed. A. Mazure, F. Casoli, F. Durret, & D. Gerbal, 1
- Biviano, A., Durret, F., Gerbal, D., et al. 1996, *A&A*, 311, 95
- Biviano, A., Girardi, M., Giuricin, G., Mardirossian, F., & Mezzetti, M. 1992, *ApJ*, 396, 35
- Biviano, A., Katgert, P., Mazure, A., et al. 1997, *A&A*, 321, 84
- Biviano, A., Maraboli, E. A., Pizzuti, L., et al. 2025, arXiv e-prints, arXiv:2508.05195
- Biviano, A., Pizzuti, L., Mercurio, A., et al. 2023a, *ApJ*, 958, 148
- Biviano, A., Pizzuti, L., Mercurio, A., et al. 2023b, *ApJ*, 958, 148
- Biviano, A., Poggianti, B. M., Jaffé, Y., et al. 2024, *ApJ*, 965, 117
- Biviano, A., Rosati, P., Balestra, L., et al. 2013, *A&A*, 558, A1
- Biviano, A. & Salucci, P. 2006, *A&A*, 452, 75–81
- Boquien, M., Burgarella, D., Roehly, Y., et al. 2019, *A&A*, 622, A103
- Boselli, A., Fossati, M., & Sun, M. 2022, *A&ARv*, 30
- Boselli, A. & Gavazzi, G. 2006, *PASP*, 118, 517–559
- Boselli, A., Voyer, E., Boissier, S., et al. 2014, *A&A*, 570, A69
- Budzynski, J. M., Koposov, S. E., McCarthy, I. G., McGee, S. L., & Belokurov, V. 2012, *MNRAS*, 423, 104–121
- Burkert, A. 1995, *ApJL*, 447, L25
- Caldwell, N., Rose, J. A., Sharples, R. M., Ellis, R. S., & Bower, R. G. 1993, *ApJ*, 106, 473
- Cha, S., Jee, M. J., Hong, S. E., et al. 2025, *ApJ*, 981, 52
- Chabrier, G. 2003, *PASP*, 115, 763–795
- Churazov, E., Khabibullin, I., Lyskova, N., Sunyaev, R., & Bykov, A. M. 2021, *A&A*, 651, A41
- Colless, M. & Dunn, A. M. 1996, *ApJ*, 458, 435
- Collister, A. A. & Lahav, O. 2005, *MNRAS*, 361, 415
- Costa, A. P., Ribeiro, A. L. B., de Moraes Neto, F. R., & dos Santos Junior, J. 2025, *Universe*, 11
- DESI Collaboration, Abdul-Karim, M., Adame, A. G., et al. 2025, arXiv e-prints, arXiv:2503.14745
- Dixon, W. J. & Mood, A. M. 1946, *J. Am. Stat. Assoc.*, 41, 557
- Dressler, A., Oemler, Jr., A., Couch, W. J., et al. 1997, *ApJ*, 490, 577–591
- Fusco-Femiano, R., Cavaliere, A., & Lapi, A. 2009, *ApJ*, 705, 1019
- Gavazzi, G., Fumagalli, M., Cucciati, O., & Boselli, A. 2010, *A&A*, 517, A73
- Gavazzi, R., Adami, C., Durret, F., et al. 2009, *A&A*, 498, L33–L36
- Geller, M. J., Diaferio, A., & Kurtz, M. J. 1999, *ApJ*, 517, L23
- Gelman, A. & Rubin, D. B. 1992, *Stat. Sci.*, 7, 457
- Gunn, J. E. & Gott, III, J. R. 1972, *ApJ*, 176, 1
- Hansen, S. H. & Moore, B. 2006, *New Astron.*, 11, 333–338
- Hernquist, L. 1990, *ApJ*, 356, 359
- Ho, M., Ntampaka, M., Rau, M. M., et al. 2022, *NatAs*, 6, 936–941
- Host, O. 2009, *Nucl. Phys. B Proc. Suppl.*, 194, 111–115
- Hwang, H. S. & Lee, M. G. 2008, *ApJ*, 676, 218
- Kang, W., Hwang, H. S., Okabe, N., & Park, C. 2025, *ApJS*, 278, 51
- Krolewski, A. & Percival, W. J. 2025, *Phys. Rev. D*, 111, 063526
- Kruskal, W. H. & Wallis, W. A. 1952, *J. Am. Stat. Assoc.*, 47, 583
- Lin, Y.-T., Mohr, J. J., & Stanford, S. A. 2004, *ApJ*, 610, 745
- Łokas, E. L. 2002, *MNRAS*, 333, 697
- Łokas, E. L. & Mamon, G. A. 2003, *MNRAS*, 343, 401–412
- Lyskova, N., Churazov, E., Zhang, C., et al. 2019, *MNRAS*, 485, 2922
- Malavasi, N., Aghanim, N., Tanimura, H., Bonjean, V., & Douspis, M. 2020, *A&A*, 634, A30
- Mamon, G. A., Biviano, A., & Boué, G. 2013, *MNRAS*, 429, 3079–3098
- Mamon, G. A., Biviano, A., & Murante, G. 2010, *A&A*, 520, A30
- Mamon, G. A., Cava, A., Biviano, A., et al. 2019, *A&A*, 631, A131
- Merritt, D. 1985, *AJ*, 90, 1027
- Mirakhor, M. S. & Walker, S. A. 2020, *MNRAS*, 497, 3204
- Moss, C. & Dickens, R. J. 1977, *MNRAS*, 178, 701
- Nagai, D., Kravtsov, A. V., & Vikhlinin, A. 2007, *ApJ*, 668, 1
- Navarro, J. F., Frenk, C. S., & White, S. D. M. 1997, *ApJ*, 490, 493–508
- Neumann, D. M., Arnaud, M., Gastaud, R., et al. 2001, *A&A*, 365, L74
- Osipkov, L. P. 1979, *Sov. Astron. Lett.*, 5, 42
- Pizzuti, L., Barrena, R., Sereno, M., et al. 2025, *A&A*, 699, A88
- Pizzuti, L., Boumechta, Y., Haridasu, S., et al. 2024, *JCAP*, 2024, 014
- Pizzuti, L., Saltas, I. D., & Amendola, L. 2021, *MNRAS*, 506, 595–612
- Pizzuti, L., Saltas, I. D., Umetsu, K., & Sartoris, B. 2022, *MNRAS*, 512, 4280
- Pizzuti, L., Sartoris, B., Borgani, S., & Biviano, A. 2020, *JCAP*, 2020, 024–024
- Read, J. I., Mamon, G. A., Vasiliev, E., et al. 2021, *MNRAS*, 501, 978
- Ribeiro, A. L. B., de Carvalho, R. R., Trevisan, M., et al. 2013, *MNRAS*, 434, 784–795
- Roberts, I. D., Parker, L. C., & Hlavacek-Larrondo, J. 2018, *MNRAS*, 475, 4704–4716
- Sampaio, V. M., de Carvalho, R. R., Aragón-Salamanca, A., et al. 2024, *MNRAS*, 532, 982–994
- Sarazin, C. L. 1980, *ApJ*, 236, 75
- Sartoris, B., Biviano, A., Rosati, P., et al. 2020, *A&A*, 637, A34
- Sato, T., Matsushita, K., Ota, N., et al. 2011, *PASJ*, 63, S991–S1007
- Singh, A., Gulati, M., & Bagla, J. S. 2019, *MNRAS*, 489, 5582
- Sodré, L. J., Capelato, H. V., Steiner, J. E., & Mazure, A. 1989, *AJ*, 97, 1279
- Sunyaev, R. A. & Zeldovich, Y. B. 1972, *Comments Astrophys. Space Phys.*, 4, 173
- Taffoni, G., Becciani, U., Garilli, B., et al. 2020, in *ASP Conf. Ser.*, ed. R. Pizzo, E. R. Deul, J. D. Mol, J. de Plaa, & H. Verkouter, Vol. 527, 307
- Tammann, G. A. 1972, *A&A*, 21, 355
- Tiret, O., Combes, F., Angus, G. W., Famaey, B., & Zhao, H. S. 2007, *A&A*, 476, L1
- Umetsu, K., Zitrin, A., Gruen, D., et al. 2016, *ApJ*, 821, 116
- Vallés-Pérez, D., Planelles, S., & Quilis, V. 2025, *A&A*, 699, A1
- Vollmer, B., Cayatte, V., Balkowski, C., & Duschl, W. J. 2001, *ApJ*, 561, 708
- White, S. D. M., Briel, U. G., & Henry, J. P. 1993, *MNRAS*, 261, L8
- Xie, L., De Lucia, G., Fossati, M., F., F., & Hirschmann. 2025, *A&A*, 698, A73
- Yahil, A. & Vidal, N. V. 1977, *ApJ*, 214, 347
- Zabludoff, A. I. & Franx, M. 1993, *AJ*, 106, 1314
- Zamani, S., Salzano, V., & Bettoni, D. 2024, *Eur. Phys. J. C*, 84, 618
- Zwicky, F. 1933, *Helv. Phys. Acta*, 6, 110

## Appendix A: Impact of the assumed number density model

For all the MG-MAMPOSS<sub>T</sub> runs discussed in the previous sections, we assumed a projected Hernquist model for the number density of member galaxies, with its scale radius  $r_v$  (we drop the superscript 'H' in this Appendix, since it is always clear what model we are using) kept as a free parameter with flat informative priors based on our preliminary fits of Sect. 2.2.

Here we want to check, using MG-MAMPOSS<sub>T</sub>, that:

- i) The projected Hernquist model is actually favoured by the MG-MAMPOSS<sub>T</sub> likelihood with respect to the NFW model.
- ii) Even if  $r_v$  is a free parameter, its best estimate is consistent with our first estimate of Sect. 2.2.
- iii) The model with  $r_v$  fixed at our best fit of Sect. 2.2 is not favoured with respect to the case in which it is a free parameter.

Table A.1 shows the details of the runs performed, with relative priors and outcomes, to check *i)–iii)*. The first two rows illustrate the comparison between projected NFW and projected Hernquist models: in these runs,  $r_v$  is a free parameter, together with  $r_{200}$ ,  $r_s$ ,  $\mathcal{A}_0$  and  $\mathcal{A}_\infty$ . For  $r_v$  we assume informative flat priors coming from our best fit estimate of Sect. 2.2, for  $r_{200}$  and  $r_s$  we use broad and flat priors, as well as for the anisotropy parameters (same as Table 1). We use the BIC and AIC criteria (Eq. 14 and 15), already used in Sect. 4.1, to evaluate the relative performance of the models. Both BIC and AIC favour the Hernquist model with respect to the NFW model: we have tested this conclusion with several runs on different samples, including the three colour classes, and mass/anisotropy models, reaching the same outcome. This validates our first assumption and excludes any systematic errors caused by the employed numerical density model.

Also our second assumption is verified by the first two rows of Table A.1: in fact, the best fit estimates of  $r_v$  from MG-MAMPOSS<sub>T</sub> are consistent with the fits performed in Sect. 2.2. Using the NFW model, the two estimates are almost exactly the same, while for the Hernquist model the best fit value is lower, but well within the  $1\sigma$  interval.

The results of the third and fourth row show what happens if we treat  $r_v$  as a fixed input parameter. In these runs, the flat priors for  $r_v$  are very tight around the best fit value from Sect. 2.2; in practice, we mimic a fixed tracer scale radius by adopting a very narrow flat prior for  $r_v$  and reduce by hand the number of free parameters by unity. The reason why we do not consider  $r_v$  as an actual fixed input parameter is that MG-MAMPOSS<sub>T</sub> uses a different expression for the fit depending on whether  $r_v$  is a fixed or free parameter (Mamon et al. 2013), invalidating the comparison of the likelihoods between the two cases. The results show that keeping  $r_v$  'fixed' with the NFW model produces an improvement of 7 BIC and 2 AIC units with respect to the free parameter case, while with the Hernquist model the BIC is improved by 4 but the AIC worsens by 2 units. Since the two criteria give conflicting indications for the adopted (Hernquist) model, we chose to treat  $r_v^H$  as a free parameter, which we consider the safest strategy.

## Appendix B: Numerical profiles for different galaxy populations

Fig. B.1 displays the projected surface density profiles of the different subsamples (RS, GV, BC) of galaxies, fitted with a pro-

jected Hernquist model. The low statistics of GV and BC samples are at the origin of the high uncertainties on the best fit scale radii (Sect. 2.2).

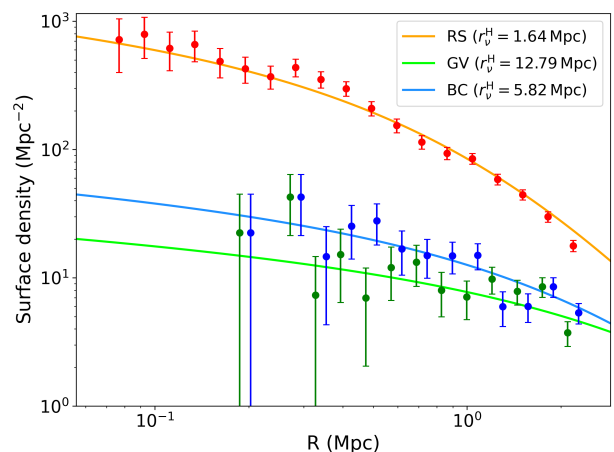


**Fig. B.1.** Surface density profiles of RS (red), GV (green), and BC (blue) galaxies in the Coma Cluster fitted with projected Hernquist models with, respectively,  $r_v^H = 1.64$  Mpc, 12.79 Mpc and 5.82 Mpc. The error bars correspond to the Poisson uncertainties.

## Appendix C: Multi-component mass profile

In Fig. C.1 we plot the total mass profile of Coma obtained by using the sample of galaxies with no distinction in the three colour classes, in the projected radial range  $R \in [0.10, 2.3]$  Mpc and assuming the multi-component mass model of eq. (16). The grey bands and the black solid line indicate the radial profile of the diffuse DM component, parametrised as a gNFW. While the virial radius (and so the dark matter mass) is well constrained,  $r_{200}^{DM} = 1.94^{+0.09}_{-0.06}$  Mpc, the scale radius  $r_s$  and the slope  $\alpha$  are completely degenerate. This is not surprising; as shown in *e.g.* Sartoris et al. (2020) and Biviano et al. (2023a), to break this degeneracy using kinematic analyses requires spectroscopic data of the stellar velocity dispersion in the BCG to be included in the fit.

## Appendix D: Mass and orbital anisotropy study for low- and high-mass galaxies

As mentioned in Sect. 4.3, we split the full sample in two equal population (662 members) stellar mass bins, with the threshold at  $\log(M_*/M_\odot) = 9.1$ , to check differences in the estimated mass and anisotropy parameters. RS galaxies are the most evenly distributed between the two bins, with 45.8% below the mass threshold and 54.2% above it. GV galaxies show a similarly balanced distribution, with 55.4% with low mass and 44.6% with high mass. In contrast, BC galaxies are strongly skewed towards the low-mass regime, where 75.3% of them are found. The colour composition of the two stellar mass bins can be found in Table D.1.

Following the same strategy adopted for the colour classes, we first ran MG-MAMPOSS<sub>T</sub> with flat priors (same as Table 1) to independently estimate the mass parameters and then we employed Gaussian priors on the mass from the joint analysis of Sect. 4.1 to compare the anisotropy profiles. The best fit parameters are reported in Table D.2 and Table D.3. Note that we

**Table A.1.** MG-MAMPOSSt priors and results for changes on tracer numerical density models.

Model	Min $r_v$ (Mpc)	Max $r_v$ (Mpc)	Best fit $r_v$ (Mpc)	$k$	$-\log \mathcal{L}$	BIC	AIC
NFW	0.59	0.86	$0.70^{+0.05}_{-0.06}$	5	12 209.84	24 455	24 429
Hernquist	1.41	2.05	$1.73^{+0.06}_{-0.16}$	5	12 207.59	24 451	24 425
NFW	0.709	0.711	0.71	4	12 209.78	24 448	24 427
Hernquist	1.929	1.931	1.93	4	12 209.56	24 447	24 427

**Notes.** The columns report, in order, the employed model for the projected number density profile, the minimum and maximum limit of the employed priors, the best fit values for  $r_v$ , the number of free parameters  $k$ , the minimum value for the negative log-likelihood, the BIC and AIC parameters. The number of free parameters for the third and fourth rows was decreased by one to mimic a constant value for  $r_v$ .

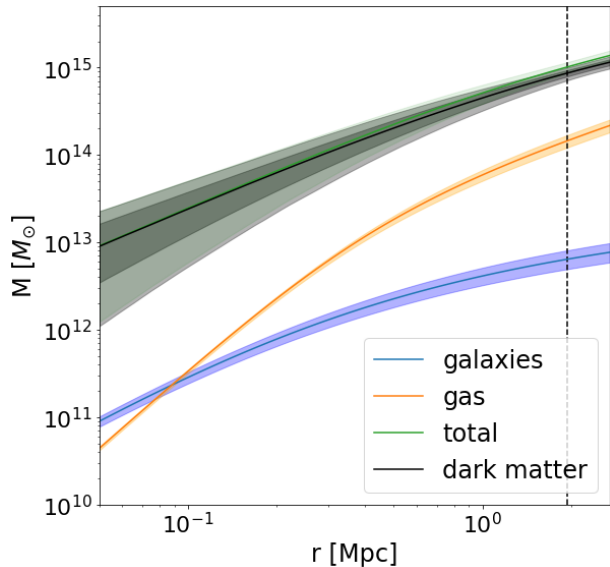


**Fig. C.1.** Total mass profile (green solid line) of Coma with its 95% confidence interval (green shaded region), along with the mass of the different components: galaxies (blue), gas (orange), DM (black). The grey inner and outer shaded regions indicate the 68% and 95% confidence region of the DM profile, respectively. The black dashed vertical line corresponds to  $r_{200}^{\text{DM}} = 1.94^{+0.09}_{-0.06}$  Mpc. The orange and blue bands represent the 68% limits of the gas and galaxies mass profiles.

**Table D.1.** Fraction of RS, GV and BC galaxies in the two stellar-mass bins.

Population	$\log(M_*/M_\odot) < 9.1$	$\log(M_*/M_\odot) > 9.1$
RS	71.6%	85.3%
GV	10.9%	8.9%
BC	17.5%	5.8%

have repeated the numerical density profile fit for these new subclasses (as in Sect. 2.2), to ensure that Gaussian priors on  $r_v^{\text{H}}$  are appropriate, finding the best fit values of  $r_v^{\text{H}} = 1.70^{+0.03}_{-0.61}$  Mpc for the low-mass and  $r_v^{\text{H}} = 1.98^{+0.41}_{-0.11}$  Mpc for the high-mass galaxies.

As expected, the mass parameters ( $r_s$  and  $r_{200}$ ) estimated from the low-mass sample are higher than those obtained from the high-mass one, given the contribute of the vast majority of BC galaxies. Both the anisotropy profiles (Fig. D.1) show a pre-

**Table D.2.** Best fit parameters for low-mass and high-mass galaxies.

Parameter	Low-mass	High-mass
$r_{200}$ (Mpc)	$2.23^{+0.10}_{-0.12}$	$2.13^{+0.06}_{-0.09}$
$r_s$ (Mpc)	$0.82^{+0.55}_{-0.52}$	$0.58^{+0.10}_{-0.35}$
$r_v^{\text{H}}$ (Mpc)	$2.09^{+0.22}_{-0.28}$	$1.35^{+0.20}_{-0.10}$
$\mathcal{A}_0$	$1.42^{+0.63}_{-0.51}$	$1.14^{+0.92}_{-0.42}$
$\mathcal{A}_\infty$	$1.20^{+0.25}_{-0.32}$	$1.42^{+0.14}_{-0.47}$

**Notes.** The employed mass and anisotropy models are NFW and gOM, respectively. The assumed priors, for these runs, are broad and flat, except for  $r_v^{\text{H}}$ , for which we considered informative priors based on the best fit values for each subsample.

**Table D.3.** Same as Table D.2, but for the runs with Gaussian priors on  $r_{200}$  and  $r_s$  from the joint analysis of Sect. 4.1.

Parameter	Low-mass	High-mass
$r_{200}$ (Mpc)	$2.18^{+0.04}_{-0.05}$	$2.13^{+0.03}_{-0.06}$
$r_s$ (Mpc)	$0.69^{+0.03}_{-0.32}$	$0.57^{+0.04}_{-0.26}$
$r_v^{\text{H}}$ (Mpc)	$1.91^{+0.18}_{-0.11}$	$1.44^{+0.16}_{-0.09}$
$\mathcal{A}_0$	$1.12^{+0.61}_{-0.47}$	$1.25^{+0.97}_{-0.54}$
$\mathcal{A}_\infty$	$1.23^{+0.13}_{-0.29}$	$1.27^{+0.17}_{-0.27}$

**Notes.** Gaussian priors on  $r_v^{\text{H}}$  are based on the estimates of Sect. 2.2, while those for  $\mathcal{A}_0$  and  $\mathcal{A}_\infty$  are flat (same as Table 1).

dominant radial component, with the high-mass galaxies showing an even more radial behaviour.

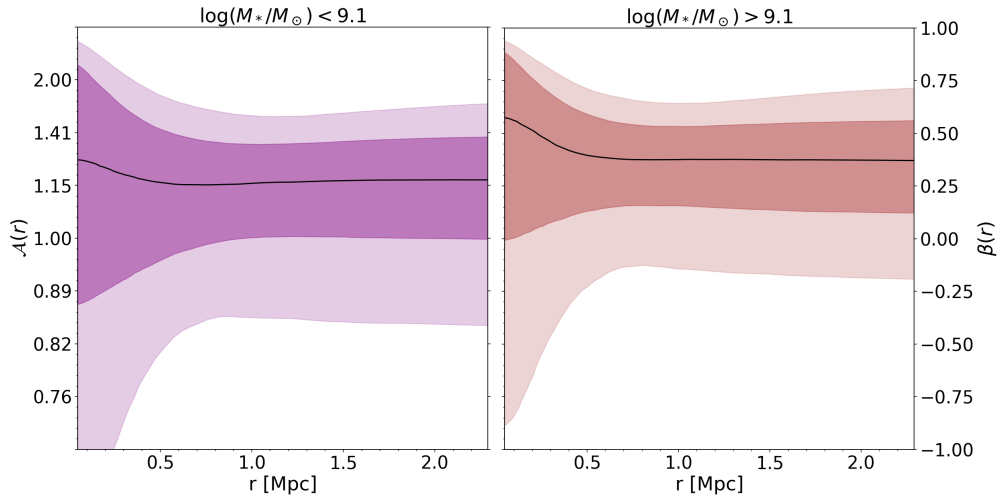


**Fig. D.1.** Estimated anisotropy profiles in NFW gOM runs with Gaussian priors on the mass (coming from the joint results of Sect. 4.1) for low-mass (left) and high-mass (right) galaxies, separately. The coloured and shaded regions indicate  $1\sigma$  and  $2\sigma$  confidence intervals, respectively. Solid curves are the median profiles of each MCMC chain.